

Near-degeneracy of several pairing channels in multiorbital models for the Fe-pnictides

S. Graser,¹ T. A. Maier,² P. J. Hirschfeld,¹ and D. J. Scalapino³

¹*Department of Physics, University of Florida, Gainesville, FL 32611, U.S.A.*

²*Center for Nanophase Materials Sciences and Computer Science and Mathematics Division, Oak Ridge National Laboratory, Oak Ridge, TN 37831-6494*

³*Department of Physics, University of California, Santa Barbara, CA 93106-9530 USA*

(Dated: May 31, 2018)

Weak-coupling approaches to the pairing problem in the iron pnictide superconductors have predicted a wide variety of superconducting ground states. We argue here that this is due both to the inadequacy of certain approximations to the effective low-energy band structure, and to the natural near-degeneracy of different pairing channels in superconductors with many distinct Fermi surface sheets. In particular, we review attempts to construct two-orbital effective band models, the argument for their fundamental inconsistency with the symmetry of these materials, and compare the dynamical susceptibilities of two and five-orbital tight-binding models. We then present results for the magnetic properties, pairing interactions, and pairing instabilities within a five-orbital tight-binding Random Phase Approximation model. We discuss the robustness of these results for different dopings, interaction strengths, and variations in band structure. Within the parameter space explored, an anisotropic, sign-changing s -wave (A_{1g}) state and a $d_{x^2-y^2}$ (B_{1g}) state are nearly degenerate, due to the near nesting of Fermi surface sheets.

PACS numbers: 74.70.-b,74.25.Ha,74.25.Jb,74.25.Kc

I. INTRODUCTION

The undoped Fe-pnictides are semi-metallic materials which exhibit structural and spin density wave (SDW) antiferromagnetic transitions. Photoemission¹ and density functional theory (DFT) calculations^{2,3,4,5} find that over an energy range near the Fermi energy the electron bands are made of states from the Fe-pnictide layers (Fig. 1) of predominantly Fe character. The two dimensional nature of these layers is such that the Fermi surfaces consist of hole cylinders around the Γ point and electron cylinders around the M point of the 2 Fe/cell Brillouin zone (see Fig. 2). In the undoped system, the near nesting of the hole and electron Fermi surfaces can give rise to a colinear antiferromagnetically ordered state within a weak coupling approximation⁶, and this state has been confirmed in neutron experiments⁷. In both the electron and hole doped cases, superconductivity appears in proximity to or coexists with the antiferromagnetic SDW order^{7,8,9,10}. It is therefore natural to consider the possibility that spin fluctuations provide the pairing mechanism and various random phase^{11,12,13,14,15} (RPA), fluctuating exchange^{16,17,18} (FLEX) and renormalization group^{19,20} calculations have been reported. These have made use of different approximations to the band structure and obtained a variety of different gap structures.

At the same time, various experimental probes of different Fe-pnictides appear to indicate quite different symmetries of the order parameter^{21,22,23,24,25,26,27,28,29,30,31,32}; as discussed below, there is a real possibility that different symmetries are realized in different materials. It is therefore important to investigate the origin of the discrepancies among the various theories with regard to their predictions for the superconducting ground state. In the case of the cuprates, where a single Cu-O hybridized band predominates at the Fermi surface, different methods and band structures all lead to d -wave pairing. If the situation is qualitatively different in the Fe-pnictides, we

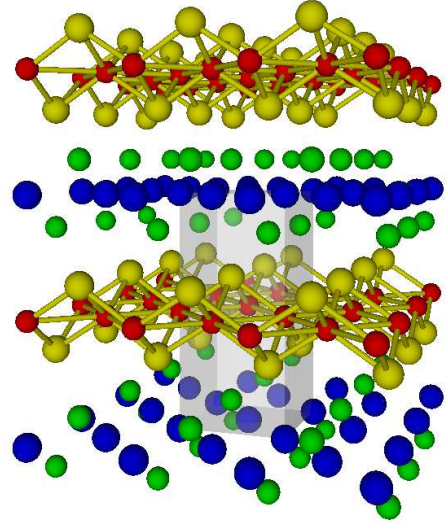


FIG. 1: (Color online) The crystal structure of LaOFeAs showing the Fe-As layers with an Fe square lattice (red) and As atoms (yellow) in a pyramidal configuration above and below the Fe plane.

need to isolate which of the apparently small differences in the various approaches is responsible for the different results obtained. The reward for such an effort may be considerable, since the evidence suggests that correlation effects in these materials may be modest compared to the cuprates, raising the possibility of a quantitative theory of the superconducting state.

Here we describe the results of an RPA calculation of the pair coupling strength and the momentum dependence of the gap function for a multiorbital tight binding parametrization of a DFT band structure for the LaOFeAs material by Cao *et*

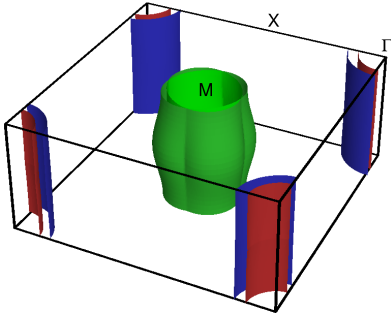


FIG. 2: (Color online) The Fermi surface for LaOFFeAs found in Ref. 4.

*al.*⁴. We begin in Sec. II by discussing the two orbital model for the electronic structure of the pnictides that was introduced by some of the present authors and has been studied by various groups, along with some of the inconsistencies associated with this approach. In Sec. III, we discuss our results for the electronic structure using a five-orbital fit to DFT. Then in Sec. IV we examine the spin and orbital susceptibilities and the effective pairing interaction for both models. In Sec. V, an effective pairing interaction strength λ and gap function $g(k)$ are introduced and in Sec. VI we discuss our results for λ and $g(k)$. In Sec. VII, we examine the spatial and orbital structure of the pairing interaction and the resulting pairs. Our conclusions and comparison with previous work are contained in the final section VIII.

II. TWO-ORBITAL MODEL

Effective models of the band structure based entirely on Fe orbitals should be possible because DFT tells us that the states due to the As 4p orbitals are located approximately 2 eV below the Fermi level. The As orbitals allow for hybridization with the Fe 3d states, however, and therefore an effective Fe-Fe hopping Hamiltonian can be constructed, provided the symmetries of the entire FeAs layer are respected. It is conceptually simplest to work therefore with a square lattice with sites corresponding to Fe atoms and introduce a set of effective hoppings between these sites. If the primitive unit cell is taken to be a square containing a single Fe atom, the effective Brillouin zone is the square shown in Fig. 3a. Since the true primitive unit cell contains two Fe atoms, the true Brillouin zone is smaller by a factor of two, as shown in Fig. 3b. The Fermi surface in the correct small zone should be obtained from the effective large zone by folding the effective zone about the black dashed lines in Fig. 3a. Sheets around the M point in Fig. 3a thus correspond to sheets around the Γ point in Fig. 3b.

In Qi *et al.*¹², a 2-orbital tight binding model was used to carry out an RPA calculation of the spin and orbital fluctuation pairing interaction. Here we briefly describe this model and discuss why it is insufficient to approximate the full band structure, especially with regard to the correct orbital weights along the Fermi surface sheets. The Hamiltonian for the two

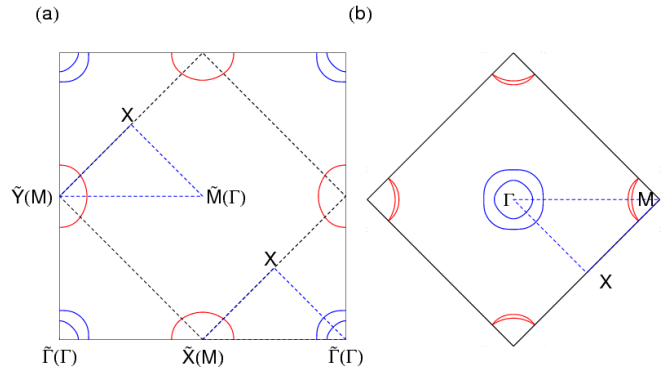


FIG. 3: (Color online) (a) Effective Brillouin zone for Fe-Fe tight-binding model; (b) Correct zone. In (a) the dashed black line shows the boundaries of the correct zone, the dashed blue lines show the two disconnected pieces of the path that have to be added to give a corresponding path in (b).

band model can be written as

$$H_0 = \sum_{k\sigma} \psi_{k\sigma}^+ [(\epsilon_+(k) - \mu) 1 + \epsilon_-(k)\tau_3 + \epsilon_{xy}(k)\tau_1] \psi_{k\sigma} \quad (1)$$

Here, τ_i are Pauli matrices and $\psi_{k\sigma}^+ = (d_{x\sigma}^+(k), d_{y\sigma}^+(k))$ is a two-component field which describes the two “ d_{xz} ” and “ d_{yz} ” orbitals. The energies $\epsilon_{\pm}(k)$ and $\epsilon_{xy}(k)$ are parameterized in terms of four hopping parameters t_i :

$$\begin{aligned} \epsilon_+(k) &= -(t_1 + t_2)(\cos k_x + \cos k_y) - 4t_3 \cos k_x \cos k_y \\ \epsilon_-(k) &= -(t_1 - t_2)(\cos k_x - \cos k_y) \\ \epsilon_{xy}(k) &= -4t_4 \sin k_x \sin k_y \end{aligned} \quad (2)$$

Diagonalizing H_0 one has

$$\psi_{s\sigma}(k) = \sum_{\nu=\pm} a_{\nu}^s(k) \gamma_{\nu\sigma}(k) \quad (3)$$

Here, $\gamma_{\nu\sigma}(k)$ destroys an electron in the $\nu = \pm$ band with spin σ and

$$\begin{aligned} a_-^x(k) &= \left[\frac{1}{2} \left(1 + \frac{\epsilon_-(k)}{\sqrt{\epsilon_-^2(k) + \epsilon_{xy}^2(k)}} \right) \right]^{\frac{1}{2}} = a_+^y(k) \\ a_+^x(k) &= \left[\frac{1}{2} \left(1 - \frac{\epsilon_-(k)}{\sqrt{\epsilon_-^2(k) + \epsilon_{xy}^2(k)}} \right) \right]^{\frac{1}{2}} = -a_+^y(k) \end{aligned} \quad (4)$$

With the addition of a chemical potential the Hamiltonian takes the following form

$$H_0 = \sum_{k\sigma} \sum_{\nu=\pm} (E_{\nu}(k) - \mu) \gamma_{\nu\sigma}^+(k) \gamma_{\nu\sigma}(k) \quad (5)$$

where the band energies are $E_{\pm}(k) = \epsilon_+(k) \pm \sqrt{\epsilon_-^2(k) + \epsilon_{xy}^2(k)}$. Measuring energy in units of $|t_1|$, for

$t_1 = -1$, $t_2 = 1.3$, $t_3 = t_4 = -0.85$ and $\mu = 1.5$ we exhibit the Fermi surface in Fig. 4, displayed in the large effective zone. To obtain the corresponding Fermi surface in the small zone, a folding across the line joining $(\pi, 0)$ and $(0, \pi)$ is required, as discussed above.

The Fermi surfaces α_1 around $(0, 0)$ and α_2 around (π, π) are hole pockets associated with $E_-(k_f) = 0$ and the β_1 and β_2 Fermi surfaces around $(\pi, 0)$ and $(0, \pi)$ are electron pockets from $E_+(k_f) = 0$. We note that the displacement of the α_2 Fermi surface from the Γ -point to (π, π) is an artifact of the 2-orbital approximation. As shown by various DFT calculations^{3,4,5} and noted by Lee and Wen³³, the orbital states that have significant weight near the β Fermi surfaces include, in addition to the d_{xz} and d_{yz} orbitals, a d_{xy} orbital. In addition, while the Fermi surface sheets shown in Fig. 4 fold down to give two hole Fermi surfaces around the Γ point of the 2Fe/cell Brillouin zone, there should in fact be two hole Fermi surfaces around the Γ point of the large, effective Brillouin zone. This is known from the wave functions found in the band structure calculations. Finally, the 2-orbital model lacks the flexibility to fit the Fermi velocities found in the band structure calculations, giving Fermi velocities on the electron β Fermi surfaces that are anomalously small compared to the velocities on the hole Fermi surfaces.

III. 5-ORBITAL MODEL

In principle, one could capture the correct behavior near the α and β Fermi surface sheets by treating a 3-orbital d_{xz} , d_{yz} , d_{xy} model. However, with short range hoppings, this leads to the appearance of an extra unphysical Fermi surface and a fourth orbital is required to remove it³³. In addition, recent theoretical calculations using 5 Wannier d-orbits per Fe site find that one can obtain an excellent representation of the electronic structure within a $\pm 2\text{eV}$ window of the Fermi energy¹¹. Furthermore, the values of the Coulomb interaction parameters obtained for the Wannier basis are such that the average Coulomb interaction is small compared to the bandwidth, implying that one is dealing with a weakly coupled system³⁴.

At this point it therefore seems best to use all five d orbitals in developing a tight-binding model¹¹. Here, using a Slater-Koster based parametrization which respects the symmetry of the FeAs layers, we fit a five-orbital (d_{xz} , d_{yz} , d_{xy} , $d_{x^2-y^2}$, and $d_{3z^2-r^2}$) tight binding model to the DFT band structure determined by Cao *et al.*⁴. We will use an orbital basis that is aligned parallel to the nearest neighbor Fe-Fe direction rather than the Fe-As direction. With this choice we avoid the necessity of introducing a second, rotated coordinate system in addition to the one that is used to describe the single Fe unit cell.

The Hamiltonian for the 5 band model takes the following form

$$H_0 = \sum_{k\sigma} \sum_{mn} (\xi_{mn}(k) + \epsilon_m \delta_{mn}) d_{m\sigma}^\dagger(k) d_{n\sigma}(k) \quad (6)$$

Here $d_{m,\sigma}^\dagger(k)$ creates a particle with momentum k and spin σ in the orbital m . The kinetic energy terms $\xi_{mn}(k)$ together

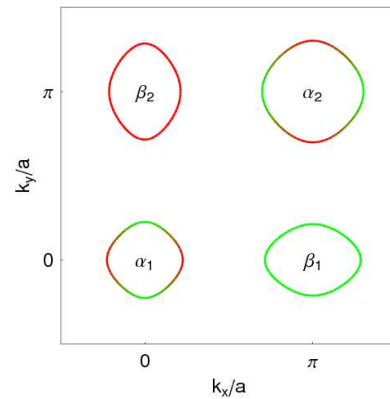


FIG. 4: (Color online) Fermi surface for the 2-orbital d_{xz} - d_{yz} model with $\mu = 1.5$ showing the α_2 FS sheet around $k = (\pi, \pi)$ rather than around $k = (0, 0)$. The orbital contributions of the band states that lie on the different FS sheets are shown color coded: d_{xz} (red) and d_{yz} (green).

with the parameters for a 5 band tight binding fit of the DFT band structure by Cao *et al.* are listed in the appendix. A diagonalization of this Hamiltonian yields the eigenenergies and the matrix elements analogously to the two band case discussed above.

In Fig. 5 (a), we have plotted the resulting band structure in the backfolded “small” Brillouin zone while the Fermi surface sheets for zero doping are shown in Fig. 5 (b). The colors correspond to the dominant orbital weight of each band in momentum space. The gray lines represent the DFT band structure by Cao *et al.* and the comparison shows, that the 5 band fit approximately reproduces the DFT bands, especially in the vicinity of the Fermi level. It is obvious that the d_{xy} contribution plays an important role in building up the electron-like Fermi surfaces (β sheets) around the M point of the “small” Brillouin zone. In the unfolded Brillouin zone (Fig. 5 (b)) the d_{xy} orbital and d_{yz} (d_{xz}) orbital contribute the dominant weights to the band states at the β_1 (β_2) Fermi surface. To confirm this we also show the orbital weights as a function of the winding angle on the different Fermi surfaces in Fig. 6.

IV. THE SPIN AND CHARGE SUSCEPTIBILITIES

A. Noninteracting susceptibilities

In this section we examine the RPA enhanced spin and charge susceptibilities for the multiorbital model that we introduced in the previous section. The spin operator for an orbital s is defined as

$$\vec{S}_s(q) = \frac{1}{2} \sum_{k,\alpha\beta} d_{s\alpha}^\dagger(k+q) \vec{\sigma}_{\alpha\beta} d_{s\beta}(k) \quad (7)$$

where α and β are spin indices. The spin susceptibility can then be calculated from the Matsubara spin-spin correlation

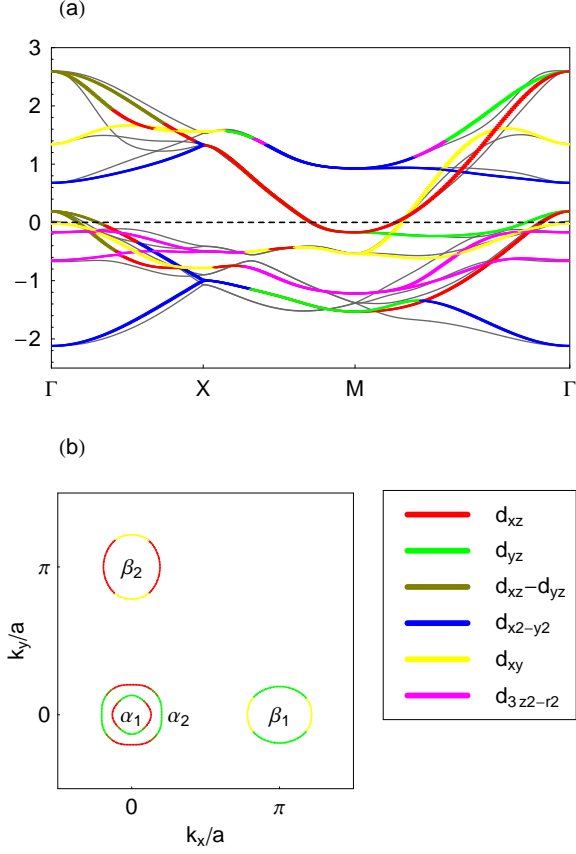


FIG. 5: (Color online) (a) The backfolded band structure for the 5 band model with Γ , X , and M denoting the symmetry points in the real Brillouin zone corresponding to the 2 Fe unit cell. The main orbital contributions are shown by the following colors: d_{xz} (red), d_{yz} (green), d_{xy} (yellow), $d_{x^2-y^2}$ (blue), $d_{3z^2-r^2}$ (magenta), and a strongly hybridized $d_{xz}-d_{yz}$ band (brown). The gray lines show the correct DFT band structure calculated by Cao *et al.* (b) The FS sheets of the 5 band model for the undoped compound ($x = 0$).

function

$$(\chi_1)_t^s(q, i\omega) = \frac{1}{3} \int_0^\beta d\tau e^{i\omega\tau} \langle T_\tau \vec{S}_s(q, \tau) \vec{S}_t(-q, 0) \rangle \quad (8)$$

with τ the imaginary time and ω a Matsubara frequency. In the same way we can define the Fourier component of the charge density for the orbital s as

$$n_s(q) = \sum_{k, \alpha\beta} d_{s\alpha}^\dagger(k+q) d_{s\beta}(k) \delta_{\alpha\beta} \quad (9)$$

and we can calculate the charge susceptibility from

$$(\chi_0)_t^s(q, i\omega) = \int_0^\beta d\tau e^{i\omega\tau} \langle T_\tau n_s(q, \tau) n_t(-q, 0) \rangle \quad (10)$$

In a more general formulation the susceptibilities are functions of four orbital indices. For the non-interacting case

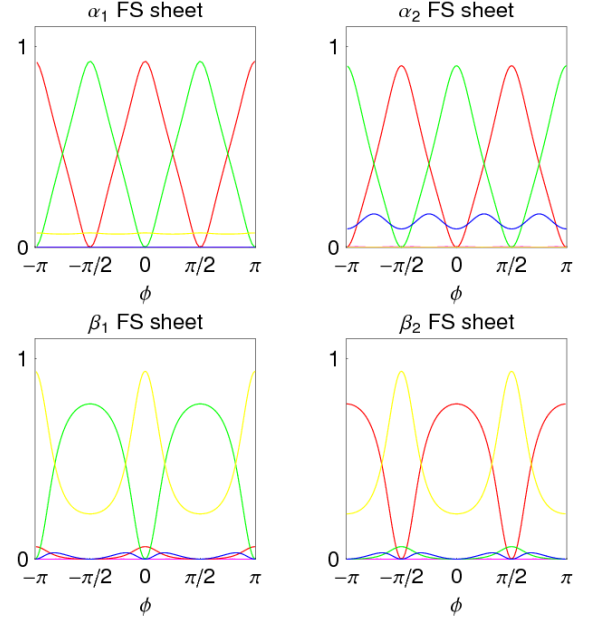


FIG. 6: (Color online) The orbital weights as a function of the winding angle ϕ on the different Fermi surface sheets. The different colors refer to d_{xz} (red), d_{yz} (green), d_{xy} (yellow), $d_{x^2-y^2}$ (blue), $d_{3z^2-r^2}$ (magenta).

$(\chi_0)_{st}^{pq}$ and $(\chi_1)_{st}^{pq}$ are equivalent and can be written

$$\chi_{st}^{pq}(q, i\omega) = \int_0^\beta d\tau e^{i\omega\tau} \sum_{kk'} \sum_{\alpha\beta} \langle T_\tau d_{p\alpha}^\dagger(k, \tau) d_{q\alpha}(k+q, \tau) d_{s\beta}^\dagger(k', 0) d_{t\beta}(k'-q, 0) \rangle \quad (11)$$

Now we can derive an explicit expression for the non-interacting susceptibilities from

$$\chi_{st}^{pq}(q, i\omega) = -\frac{1}{N\beta} \sum_{k, i\omega_n} G_{sp}(k, i\omega_n) G_{qt}(k+q, i\omega_n + i\omega) \quad (12)$$

where N is the number of Fe lattice sites, $\beta = 1/T$, and the spectral representation of the Green's function is given as

$$G_{sp}(k, i\omega_n) = \sum_{\mu} \frac{a_{\mu}^s(k) a_{\mu}^{p*}(k)}{i\omega_n - E_{\mu}(k)} \quad (13)$$

Here the matrix elements $a_{\mu}^s(k) = \langle s | \mu k \rangle$ connect the orbital and the band space and are the components of the eigenvectors resulting from the diagonalization of the initial Hamiltonian. Performing the Matsubara frequency summation and setting $i\omega_n \rightarrow \omega + i0^+$ we find the retarded susceptibility

$$\chi_{st}^{pq}(q, \omega) = -\frac{1}{N} \sum_{k, \mu\nu} \frac{a_{\mu}^s(k) a_{\mu}^{p*}(k) a_{\nu}^q(k+q) a_{\nu}^{t*}(k+q)}{\omega + E_{\nu}(k+q) - E_{\mu}(k) + i0^+} \times [f(E_{\nu}(k+q)) - f(E_{\mu}(k))] \quad (14)$$

B. Random phase approximation for multiorbital system

Now we consider Coulomb interactions of the electrons on the same Fe atom in an RPA framework. We distinguish between an intraorbital interaction U of electrons in the same orbital and an interorbital interaction of electrons in different orbitals V . We can also take the Hund's rule coupling into account that favors the parallel alignment of electron spins on the same ion and is described by an energy $J > 0$ and the pair hopping energy denoted by J' . These interactions are generated automatically in multiorbital models with general two-body interactions using a Hubbard-type approach restricted to intrasite processes^{35,36,37}. Thus in general one can write

$$H_{int} = U \sum_{is} n_{i,s\uparrow} n_{i,s\downarrow} + \frac{V}{2} \sum_{i,s,t \neq s} n_{is} n_{it} - \frac{J}{2} \sum_{i,s,t \neq s} \vec{S}_{is} \cdot \vec{S}_{it} + \frac{J'}{2} \sum_{i,s,t \neq s} \sum_{\sigma} c_{i,s\sigma}^{\dagger} c_{i,s\bar{\sigma}}^{\dagger} c_{i,t\bar{\sigma}} c_{i,t\sigma} \quad (15)$$

where $n_{is} = n_{i,s\uparrow} + n_{i,s\downarrow}$. We have separated the intraorbital exchange J and ‘‘pair hopping’’ term J' for generality, but note that if they are generated from a single two-body term they are related by $J' = J/2$. If we now split the interaction Hamiltonian into singlet ($H_{int}^{(s)}$), triplet ($H_{int}^{(t)}$) and pair ($H_{int}^{(p)}$) channels, we find

$$H_{int}^{(s)} = \sum_{i,st} \left[\frac{U}{4} \delta_{st} + \frac{V}{2} (1 - \delta_{st}) \right] n_{is} n_{it} \quad (16)$$

and

$$H_{int}^{(t)} = - \sum_{i,st} \left[\frac{U}{12} \delta_{st} + \frac{J}{8} (1 - \delta_{st}) \right] \vec{\sigma}_{is} \vec{\sigma}_{it} \quad (17)$$

where $\vec{\sigma}_{is} = 2\vec{S}_{is}$, as well as

$$H_{int}^{(p)} = \sum_{i,st} \sum_{\sigma} \frac{J'}{2} (1 - \delta_{st}) c_{i,s\sigma}^{\dagger} c_{i,s\bar{\sigma}}^{\dagger} c_{i,t\bar{\sigma}} c_{i,t\sigma} \quad (18)$$

The RPA susceptibilities are obtained in the form of Dyson-type equations as

$$(\chi_0^{RPA})_{st}^{pq} = \chi_{st}^{pq} - (\chi_0^{RPA})_{uv}^{pq} (U^c)_{wz}^{uv} \chi_{st}^{wz} \quad (19)$$

and

$$(\chi_1^{RPA})_{st}^{pq} = \chi_{st}^{pq} + (\chi_1^{RPA})_{uv}^{pq} (U^s)_{wz}^{uv} \chi_{st}^{wz}, \quad (20)$$

where repeated indices are summed over. Here the non-zero components of the matrices U^c and U^s are given as

$$(U^c)_{aa}^{aa} = U, (U^c)_{bb}^{aa} = 2V, (U^c)_{ab}^{ab} = \frac{3}{4}J - V, (U^c)_{ab}^{ba} = J'$$

and

$$(U^s)_{aa}^{aa} = U, (U^s)_{bb}^{aa} = \frac{1}{2}J, (U^s)_{ab}^{ab} = \frac{1}{4}J + V, (U^s)_{ab}^{ba} = J'$$

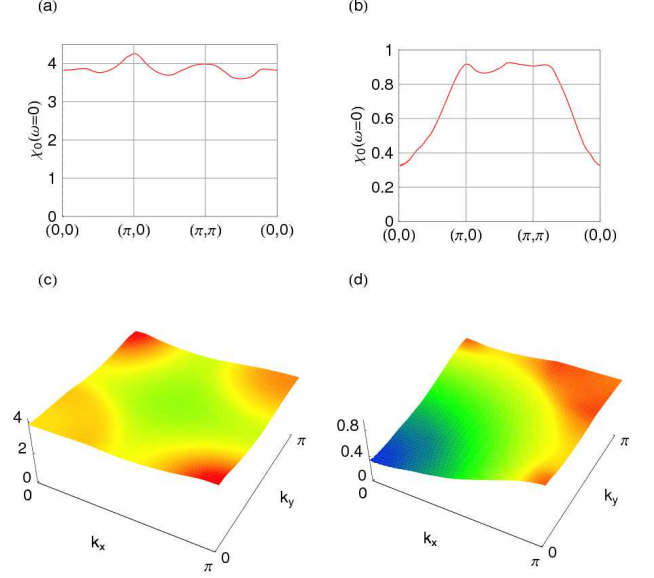


FIG. 7: (Color online) The bare spin susceptibility $\chi_S(q)$ calculated for the undoped 5 orbital model without (a,c) and with (b,d) the matrix elements. While (a) and (b) show cuts of the susceptibility along the main symmetry directions, (c) and (d) show the susceptibility in the first quadrant of the effective Brillouin zone.

where $a \neq b$. Our notation of the interaction parameters U , V , J and J' can be compared to the notation in Kubo³⁷ as

$$\tilde{U} = U, \tilde{U}' = V + \frac{J}{4}, \tilde{J} = \frac{J}{2}, \tilde{J}' = J' \quad (21)$$

where \tilde{U} , \tilde{V} , \tilde{J} and \tilde{J}' denote the interaction parameters introduced in Ref. 37. In Fig. 7 we show results for the static, homogeneous bare spin susceptibility

$$\chi_S(\mathbf{q}) = \frac{1}{2} \sum_{sp} (\chi_1)_{ss}^{pp}(\mathbf{q}, 0) \quad (22)$$

as a function of \mathbf{q} in the first quadrant of the effective ‘‘large’’ Brillouin zone as well as cuts along the main symmetry directions. We compare calculations that have been performed correctly including the matrix elements to calculations where the matrix elements have been considered to be constant $a_{\mu}^s(k) a_{\mu}^{p*}(k) = 1/5$, as has been reported in certain *ab initio* electronic structure calculations. Here we used the five band fit discussed in the previous section and chose a chemical potential that corresponds to the undoped compound ($x = 0$). As can be seen from Fig. 7 the matrix elements play a very important role by ‘‘filtering’’ special structures of $\chi_S(q)$ in momentum space, e.g. suppressing the weight for small q . The matrix elements for the $d_{x^2-y^2}$ and $d_{3z^2-r^2}$ are very small on the Fermi surfaces (Fig. 6) so that the actual $\chi_S(q)$ is reduced when these matrix elements are properly taken into account. Neglecting the matrix elements will lead to a wrong result and generally to a higher value and more homogeneous

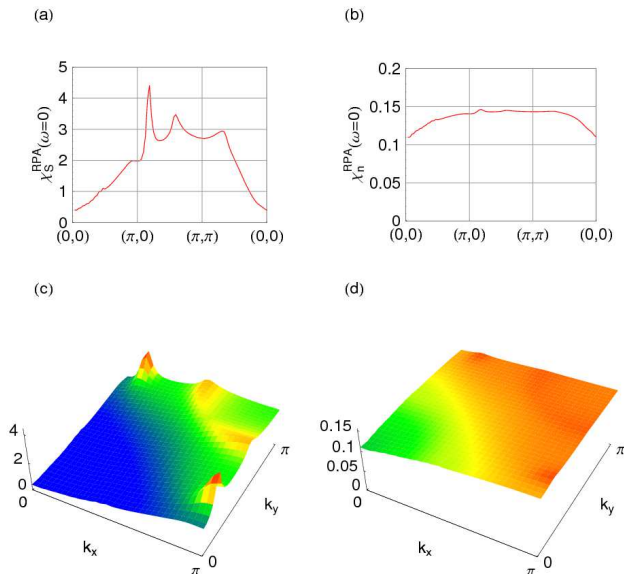


FIG. 8: (Color online) The RPA enhanced susceptibilities calculated for the electron-doped compound ($x = 0.125$). The interaction parameters have been chosen as $U = V = 1.65$ and $J = 0$. (a) and (c) are plots of the spin susceptibility, (b) and (d) are plots of the charge susceptibility.

distribution of the susceptibility in momentum space. Important features like the $Q = (\pi, 0)$ -peak, that is responsible for the antiferromagnetic SDW instability, can be under- or over-estimated.

For the single band susceptibility the inclusion of interactions within an RPA approach is known to enhance existing structures in the bare susceptibility as $U\chi'_0(q)$ approaches 1. In the case of a multiorbital susceptibility with onsite intra-orbital repulsion U , onsite interorbital repulsion V and Hund's rule coupling J it is not obvious how the different structures in the spin and in the charge susceptibility are changed by the variation of these three parameters. For a simplified and more transparent discussion we will first study the susceptibility as a function of U and we will choose $V = U$ and $J = J' = 0$. In Fig. 8 we compare the spin and charge susceptibilities of the electron-doped compound with $x = 0.125$ for a value of $U = 1.65$ that is chosen such that the main peaks in the spin susceptibility are considerably enhanced. Here, as elsewhere in this paper, energy units are in eV. For this value of U we find that the charge susceptibility is more than one order of magnitude smaller than the spin susceptibility. In addition the charge susceptibility has no pronounced structures in momentum space whereas the spin susceptibility shows two distinct peaks between $(\pi, 0)$ and (π, π) . While in the undoped compound (see Fig. 7) we find the main peak in the spin susceptibility at the antiferromagnetic wave vector $Q = (\pi, 0)$ (corresponding to (π, π) in the “small” BZ) we observe a shift of this peak towards an incommensurate wave vector $Q^* = (\pi, 0.16\pi)$ in the electron-doped com-

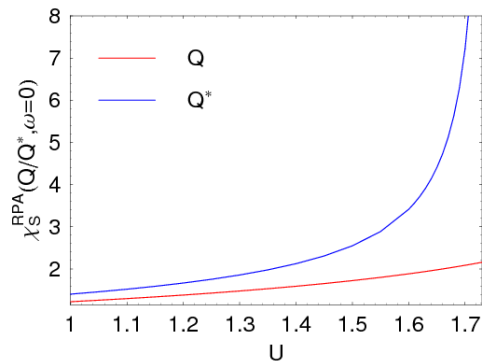


FIG. 9: (Color online) The RPA enhanced spin susceptibility $\chi_S(Q, \omega = 0)$ as a function of the interaction strength $U = V$ for the electron-doped compound ($x = 0.125$) at two different momenta $Q = (\pi, 0)$ and $Q^* = (\pi, 0.16\pi)$.

ound ($x = 0.125$). This shift can be attributed to an imperfect nesting of the α and β FS sheets due to the opposite growth of the electron and hole sheets with doping.

When we finally compare in Fig. 9 the change of the spin susceptibility as a function of U for the antiferromagnetic wave vector $Q = (\pi, 0)$ to the one for the incommensurate wave vector $Q^* = (\pi, 0.16\pi)$ we find a moderate and nearly linear increase of $\chi_S(Q)$ while $\chi_S(Q^*)$ diverges if we approach the critical value of U .

C. T dependence of χ and $(T_1T)^{-1}$

The temperature dependence of the magnetic susceptibility and NMR spin-lattice relaxation rate in the paramagnetic phase are immediate tests of our RPA calculation of $\chi_S(\mathbf{q}, \omega)$. The susceptibility of the F-doped LaOFeAs 1111 material which we study here has been measured both by direct magnetization and NMR methods^{38,39,40} and found to increase quasi-linearly up to several hundred degrees K. In addition, Zhang *et al.* have pointed out that this behavior appears to hold for the 122 class of materials as well, and that the slope of the linear- T behavior appears to be roughly doping-independent⁴¹. Within our theory, we can calculate the homogeneous, static bare spin susceptibility by summing over spins and using Eq. 22. At $T = 0$ it reduces to

$$\chi_0 \equiv 2\chi_S = 2 \sum_{\nu} N_{\nu}(0), \quad (23)$$

which is of course just the Pauli susceptibility proportional to the total density of states at the Fermi level ($N_{\nu}(0)$ is the single-spin density of states at the Fermi level in band ν). At finite temperatures one might assume that the susceptibility of an itinerant electron system should decrease. This is the usual case for a single parabolic band, but in the presence of band structure effects the susceptibility may first increase. For example, in a single band system the band structure enters in a simple way as $\chi_0(T) \sim \chi_0(0) + [(N''(0)N(0) - N'(0)^2)/N(0)^2]T^2$, where N' , N'' , are the derivatives of the

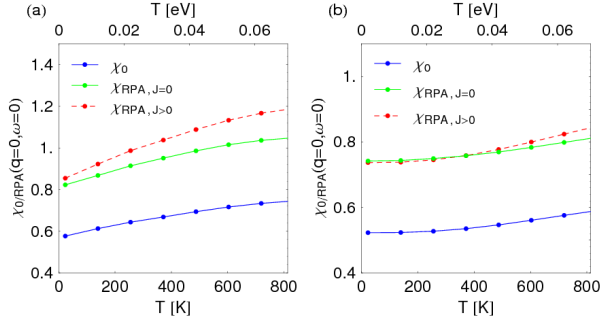


FIG. 10: (Color online) The susceptibility $\chi_0(T) = 2\chi_S(\mathbf{q} = 0, \omega = 0; T)$ (blue) in units of $\text{eV}^{-1}\text{Fe}^{-1}$ vs. T in Kelvin for a doping of $x = 0$ (a) and $x = 0.125$ (b). The interaction parameters have been chosen to be $U = 1.1, J' = 0.25U$ (red) and $J = J' = 0, U = V = 1.35$ (a) or $U = V = 1.5$ (b), respectively (green).

density of states at the Fermi level. Our situation is also somewhat unusual as the chemical potential sits in a region of rapidly varying density of states, so one may expect the T dependence of the susceptibility to differ from the textbook results.

We now plot in Fig. 10 the temperature dependence of both χ_0 and the RPA enhanced χ for the undoped and doped cases, for a particular choice of interaction parameters. It is seen that in both the doped and undoped cases, the susceptibility indeed increases quasilinearly over the experimentally interesting range of 100 to 500K. This qualitative result appears to be relatively independent of the choice of interaction parameters since it arises from the band structure. The RPA enhancement for the cases shown is of order 30%. While this factor increases as one approaches the critical U at which the Stoner instability is reached, it cannot increase dramatically, because for the electronic structure of the current model, the instability at large q occurs first. Thus a large enhancement (Ref. 42) of the $q = (0, 0)$ susceptibility does not occur in this model. We conclude that the observed susceptibility contains a significant temperature-independent interband or van Vleck component which is not included in the χ_S calculated here. Similar conclusions were reached by the authors of Ref. 39.

We also calculated the NMR relaxation rate $1/(T_1T)$ that is proportional to the imaginary part of the local (q integrated) spin susceptibility

$$\frac{1}{T_1T} = \frac{1}{N} \sum_q |A(q)|^2 \frac{\text{Im}[\chi(q, \omega_L, T)]}{\omega_L} \quad (24)$$

where $A(q)$ is a geometrical structure factor and ω_L is the NMR frequency. In Fig 11 we show $1/(T_1T)$ as a function of temperature for the same set of parameters that we have used for the $q = 0$ susceptibility. Here we find for the interacting system an initial decrease of the relaxation rate as a function of temperature that is most significant for the undoped compound with finite values of J . In the latter case we find a very distinct upturn around 300 K followed by a slight and nearly linear increase. For the other cases we find a similar tendency, although not as pronounced. In panels 11 (a)

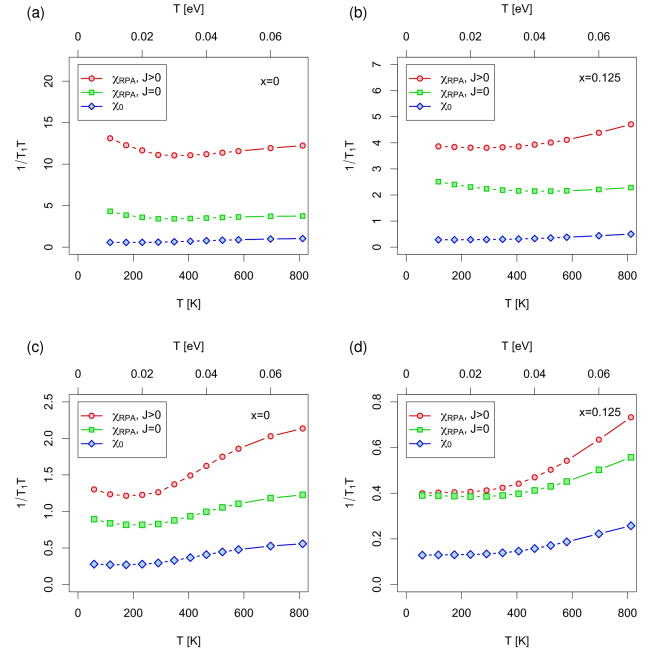


FIG. 11: (Color online) The NMR relaxation rate in units of $\text{eV}^{-2}\text{Fe}^{-1}$ as a function of temperature T for two different dopings and with the same set of interaction parameters and line colors as in Fig. 10. Panels (a) and (b) represent $x = 0$ and $x = 0.125$, respectively, for form factor $A(\mathbf{q}) = 1$. Panels (c) and (d) represent $x = 0$ and $x = 0.125$ for $A(\mathbf{q}) = \cos q_x/2 \cos q_y/2$.

and (b) we take the hyperfine form factor of the ^{19}F nucleus used e.g. in Ref. 40 to be constant, since the F is located directly above the Fe in the LOFFA material. In panels (c) and (d), we have modelled the form factor of the ^{75}As nucleus as $A(\mathbf{q}) = \cos q_x/2 \cos q_y/2$, which suppresses the $(\pi, 0)$ fluctuations, since the As atom is in the center of a square containing four Fe.

Figures 10 and 11 are intended to show some of the dependence of the susceptibility and T_1^{-1} on interaction parameters for a few cases. The trends are qualitatively similar to experiments^{38,39,40}, although the increase with increasing temperature for both quantities found here is somewhat weaker than observed. We have not attempted to fit experiments in detail.

V. THE EFFECTIVE INTERACTION AND THE GAP FUNCTION

Assuming that the pairing interaction responsible for the occurrence of superconductivity in the iron pnictides arises from the exchange of spin and charge fluctuations, we can calculate the pairing vertex using the fluctuation exchange approximation⁴³. For the multi-orbital case³⁶, the singlet pairing

vertex is given by

$$\Gamma_{st}^{pq}(k, k', \omega) = \left[\frac{3}{2} U^s \chi_1^{RPA}(k - k', \omega) U^s + \frac{1}{2} U^s - \frac{1}{2} U^c \chi_0^{RPA}(k - k', \omega) U^c + \frac{1}{2} U^c \right]_{ps}^{tq} \quad (25)$$

The χ_1^{RPA} term describes the spin fluctuation contribution and the χ_0^{RPA} term the orbital (charge) fluctuation contribution. Fig. 12 shows the Matsubara frequency dependence of these two terms for a momentum transfer $(\pi, 0)$ and a typical interaction strength. Here one sees that the spin fluctuation contribution is dominant and falls off on a frequency scale which is small compared with the bandwidth. Thus while the gap equation depends upon the kernel $\text{Im}\Gamma_{st}^{pq}(k, k', \omega)$, the important k and k' values are restricted by this frequency cut-off to remain near the Fermi surfaces. Then, just as for the electron-phonon case, the strength of the pairing interaction is characterized by a frequency integral of this kernel weighted by ω^{-1} . Making use of the Kramers-Kronig relation

$$\int_0^\infty d\omega \frac{\text{Im}[\Gamma_{st}^{pq}(k, k', \omega)]}{\pi\omega} = \text{Re}[\Gamma_{st}^{pq}(k, k', \omega = 0)] \quad (26)$$

we can proceed further by considering only the real part of the $\omega = 0$ pairing interaction. If we now confine our considerations to the vicinity of the Fermi surfaces we can determine the scattering of a Cooper pair from the state $(k, -k)$ on the Fermi surface C_i to the state $(k', -k')$ on the Fermi surface C_j from the projected interaction vertex

$$\Gamma_{ij}(k, k') = \sum_{stpqr} a_{\nu_i}^{t,*}(-k) a_{\nu_i}^{s,*}(k) \text{Re}[\Gamma_{st}^{pq}(k, k', 0)] \times a_{\nu_j}^p(k') a_{\nu_j}^q(-k') \quad (27)$$

where the momenta k and k' are restricted to the different Fermi surface sheets with $k \in C_i$ and $k' \in C_j$. If we decompose the superconducting gap into an amplitude Δ and a normalized symmetry function $g(k)$ we can define a dimensionless pairing strength functional⁴⁴ as

$$\lambda[g(k)] = - \frac{\sum_{ij} \oint_{C_i} \frac{dk_{\parallel}}{v_F(k)} \oint_{C_j} \frac{dk'_{\parallel}}{v_F(k')} g(k) \Gamma_{ij}(k, k') g(k')}{(2\pi)^2 \sum_i \oint_{C_i} \frac{dk_{\parallel}}{v_F(k)} [g(k)]^2} \quad (28)$$

Here Γ_{ij} is only the symmetric part

$$\frac{1}{2} [\Gamma_{ij}(k, k') + \Gamma_{ij}(k, -k')] \quad (29)$$

of the full interaction, which gives identical results within the spin singlet subspace. The Fermi velocity is defined to be $v_F(k) = |\nabla_k E_\nu(k)|$ for k on the given Fermi surface. From the stationary condition we find the following eigenvalue problem

$$- \sum_j \oint_{C_j} \frac{dk'_{\parallel}}{2\pi} \frac{1}{2\pi v_F(k')} \Gamma_{ij}(k, k') g_\alpha(k') = \lambda_\alpha g_\alpha(k) \quad (30)$$

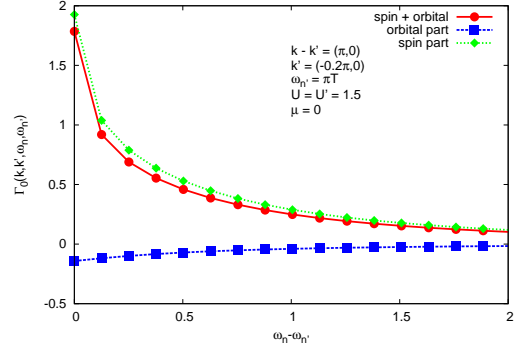


FIG. 12: (Color online) The energy dependence of the spin and orbital part of the effective pairing interaction $\Gamma(k, k', \omega_n, \omega'_n)$.

The kernel $\Gamma_{ij}(k, k')$ is evaluated at temperatures well below the characteristic temperature at which the spin fluctuation spectrum has formed. In this temperature region, the interaction is independent of temperature. From the above eigenvalue problem we will determine the leading eigenfunction $g_\alpha(k)$ and eigenvalue λ_α for a given interaction vertex $\Gamma_{ij}(k, k')$. The largest eigenvalue will lead to the highest transition temperature and its eigenfunction determines the symmetry of the gap. The next leading eigenvalues and eigenfunctions further characterize the pairing interaction and can indicate the structure of possible collective states. With the knowledge of the pairing function $g_\alpha(k)$ we can also determine the individual contributions of the different intra- and interorbital scattering processes to the total pairing strength λ_α .

VI. RESULTS FOR THE PAIRING STRENGTH λ AND THE GAP FUNCTION $g(k)$

A. Eigenvalue problem

In this section, we present and discuss results for the pairing strength λ and the symmetry function $g(k)$ obtained within our weak-coupling approach.

Solving the eigenvalue problem given in Eq. 30, we find a set of eigenfunctions $g_\alpha(k)$ defining the k dependence of the gap on the FS sheets together with a set of corresponding eigenvalues λ_α denoting the dimensionless pairing strengths associated with a given $g_\alpha(k)$. We first have to classify the different eigenfunctions according to basic symmetry operations. In the following we will speak of an s wave state if

$$\begin{aligned} g(-k_x, k_y) &= g(k_x, -k_y) = g(k_x, k_y) \\ g(k_y, k_x) &= g(k_x, k_y) \end{aligned} \quad (31)$$

while we have a $d_{x^2-y^2}$ wave state if

$$\begin{aligned} g(-k_x, k_y) &= g(k_x, -k_y) = g(k_x, k_y) \\ g(k_y, k_x) &= -g(k_x, k_y) \end{aligned} \quad (32)$$

Since there are two different $d_{x^2-y^2}$ wave states among the first few eigenfunctions, we have to distinguish them further,

e.g. by comparing the sign of $g_\nu(k)$ for $\nu = \alpha_1$ and $\nu = \alpha_2$ in the same direction in momentum space. Here we will label the state that changes sign between α_1 and α_2 with $d_{x^2-y^2}(1)$, the one without sign change with $d_{x^2-y^2}(2)$. Furthermore we can distinguish a d_{xy} wave state that is given by

$$\begin{aligned} g(-k_x, k_y) &= g(k_x, -k_y) = -g(k_x, k_y) \\ g(k_y, k_x) &= g(k_x, k_y) \end{aligned} \quad (33)$$

and a g wave state with

$$\begin{aligned} g(-k_x, k_y) &= g(k_x, -k_y) = -g(k_x, k_y) \\ g(k_y, k_x) &= -g(k_x, k_y) \end{aligned} \quad (34)$$

B. Results: $J = J' = 0$

First we consider a case where the Hund's rule coupling and the pair hopping energy are negligible compared to the intra- and interorbital Coulomb interactions, so we set $J = J' = 0$ and $V = U$. In Fig. 13 (a) we show the pairing strength eigenvalues λ_α for the four leading eigenvalues as a function of U for the electron-doped compound ($x = 0.125$). Approaching the critical value of U where the eigenvalues start to diverge we find a clear separation of the two leading eigenvalues from the next two eigenvalues. However the two leading eigenvalues, corresponding to the s and the $d_{x^2-y^2}$ symmetry remain very similar in size and we find a crossover from the $d_{x^2-y^2}$ to the s symmetry around $U = 1.65$. We also show the s wave (d) and the $d_{x^2-y^2}$ wave (e) pairing functions on the four FS sheets for $U = 1.73$ close to its critical value⁴⁵. The extended s wave state (which we have labelled s) is characterized by i) a sign change on the β FS sheets with nodal points displaced from the generic $(0, \pi)$ - $(\pi, 0)$ direction that would result from a pure $\cos k_x + \cos k_y$ state, and ii) a change of average sign on the β sheet relative to that on the α sheets. On the α FS sheets we find a nodeless but anisotropic gap distribution with higher weight on the small α_1 compared to the larger α_2 sheet. The $d_{x^2-y^2}$ state features an anisotropic gap distribution on the β FS sheets and a rather conventional d wave gap distribution on the α FS surfaces, with a sign change between the α_1 and α_2 sheet. In Fig. 14 we show the corresponding results for the undoped ($x = 0$) compound. Here we find similar results, although the eigenvalues close to the instability are better separated and the crossover from $d_{x^2-y^2}$ to s appears already for a rather small value of U . If we compare the s wave symmetry function for $x = 0$ close to the instability (see Fig. 14 (d)) to the corresponding symmetry function for the electron-doped compound, we find that the nodal points on the β FS have moved even closer to the tips of the sheets and the negative dip between them has decreased considerably. For the $d_{x^2-y^2}$ symmetry (see Fig. 14 (e)) we find that the weight on the α_2 FS sheet has nearly vanished.

In Figs. 13 and 14, as well as in the following Figs. 16 and 15 we compare in panels (b) and (c) the contributions of the different intra- and interband processes. Here $\lambda_{\alpha\alpha}$ sums up all contributions of λ_{ij} resulting from scattering within each α sheets and in between the two α sheets as $\lambda_{\alpha\alpha} = \sum_{i,j=1,2} \lambda_{ij}$

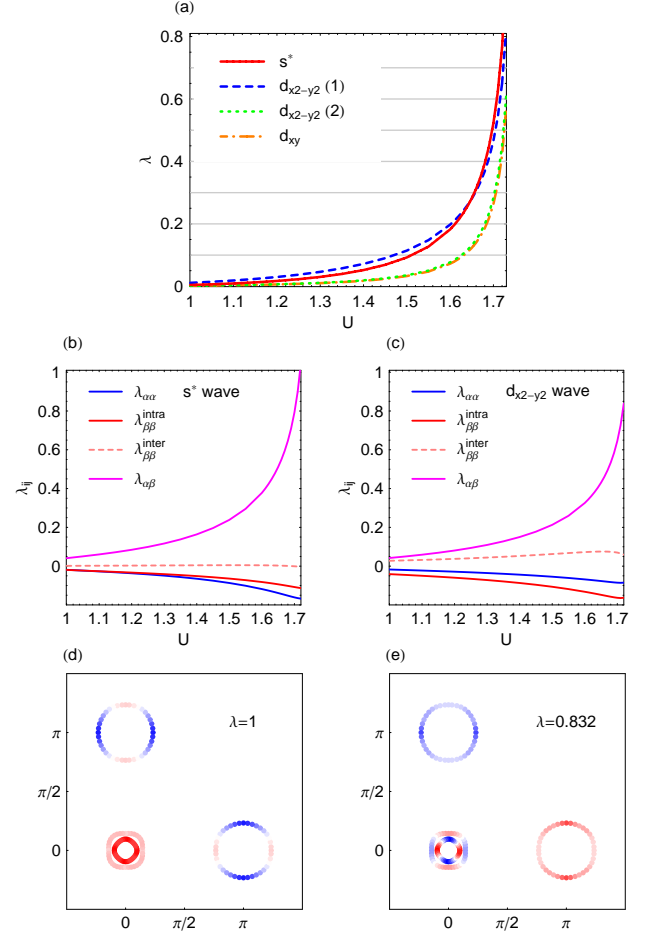


FIG. 13: (Color online) The eigenvalues and eigenfunctions for the electron-doped compound ($x = 0.125$) for $U = V$ and $J = J' = 0$. The four largest eigenvalues as a function of U (a) and the different inter- and intraband contributions to the eigenvalues λ for the two symmetries with largest eigenvalues, extended s wave (b) and $d_{x^2-y^2}$ (c) wave. Color coded plot of the extended s wave (d) and the $d_{x^2-y^2}$ wave (e) pairing functions along the different Fermi surface sheets, calculated close to the instability ($U = V = 1.73$).

where $i = 1$ refers to the α_1 , $i = 2$, to the α_2 , $i = 3$ to the β_1 and $i = 4$ to the β_2 Fermi surface. $\lambda_{\beta\beta}^{intra} = \lambda_{33} + \lambda_{44}$ denotes the intraband contributions of the β FS sheets, while $\lambda_{\beta\beta}^{inter} = \lambda_{43} + \lambda_{34}$ is the corresponding interband contribution. Finally $\lambda_{\alpha\beta}$ sums up all the remaining contributions, resulting from scattering between the α and β Fermi surfaces. It is obvious that in the case of $J = J' = 0$ for both of the main pairing symmetries the intersheet $\lambda_{\alpha\beta}$ contribution is responsible for the rapid increase of the pairing strength λ with U , reflecting the nesting between the α and β FS sheets with nesting vector Q^* . All other contributions are small and mainly negative. For finite values of J and J' , which we will next discuss we find that for the $d_{x^2-y^2}$ pairing symmetry the interorbital contributions between the two β sheets become also important and for the electron-doped compound even dominant.

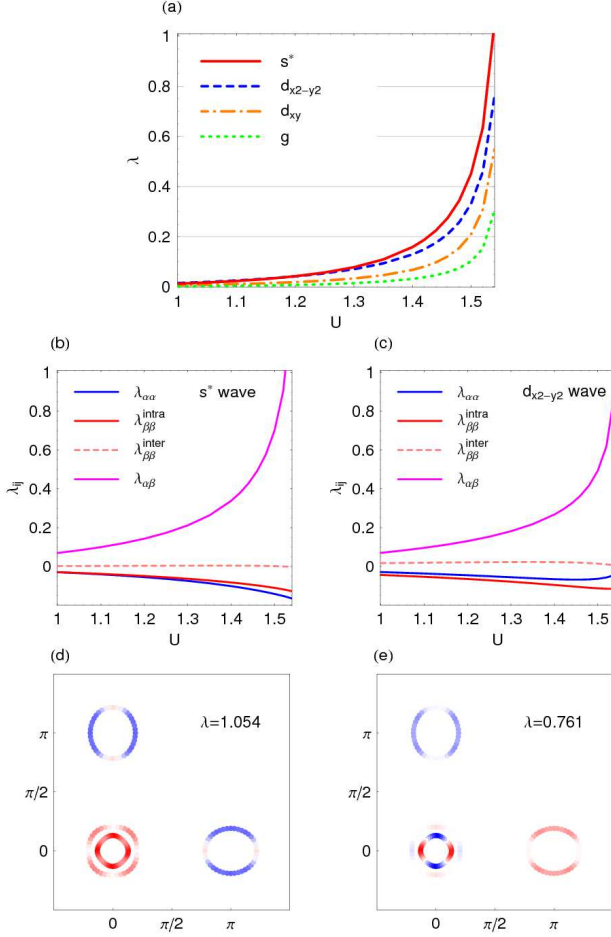


FIG. 14: (Color online) The same as in Fig. 13 but for the undoped compound ($x = 0$) with $V = U$ and $J = J' = 0$. Here the two pairing functions shown in (d,e) correspond to the two leading eigenvalues and are calculated for $U = 1.54$.

C. Results: $J, J' > 0$

Now we consider a case of finite J and J' . Here we will choose $J' = J/2$ and we will fix $V = U - 3/4J - J'$. These choices are consistent with the generation of intrasite couplings from a Hubbard argument^{35,37}, as mentioned above, as well as with the range of values for J/U found by Anisimov *et al.* in an *ab initio* calculation³⁴. In Fig. 15 (a) we show for the undoped compound ($x = 0$) and for $J' = J/2 = U/4$ the same four eigenvalues as a function of U as in the previous figures. Here we find again that the extended s wave state (d) is the most stable pairing configuration followed by the $d_{x^2-y^2}$ wave state (e). For the $d_{x^2-y^2}$ state the main contributions to the pairing function are along the β FS sheets, while the α FS sheets contribute less significantly. Since this state has no nodes along the β sheets, it can be considered as a mainly nodeless state, in contrast to the states found for $J = J' = 0$. The same is true for the electron-doped case with $x = 0.125$ (Fig. 16). Here the $d_{x^2-y^2}$ state is the most

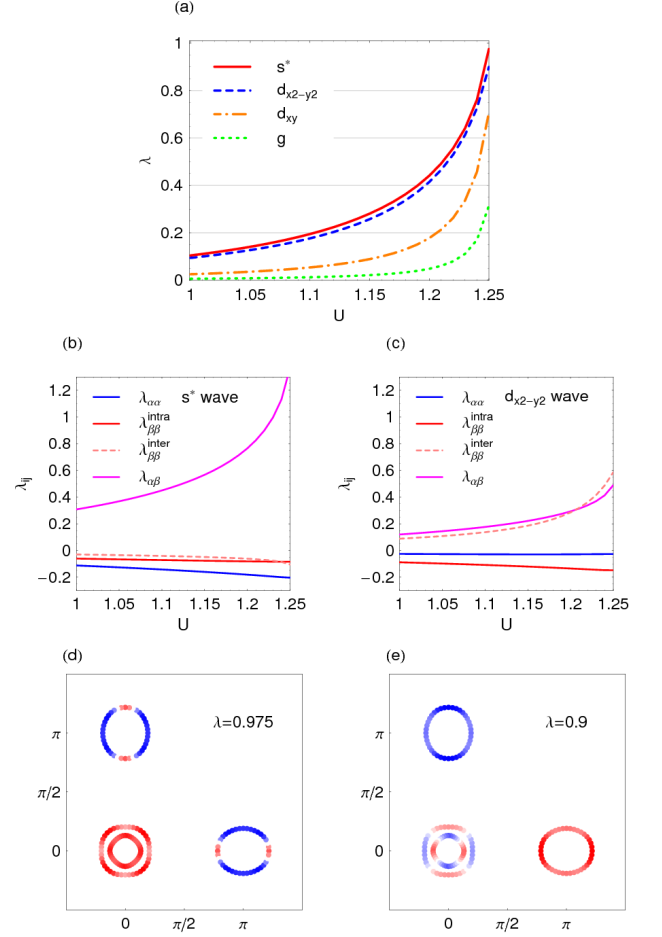


FIG. 15: (Color online) The same as in Fig. 13 for the undoped compound ($x = 0$) with $J' = J/2 = U/4$ and $V = U - 5/4J$. Again the extended s wave (d) and the $d_{x^2-y^2}$ wave (e) pairing functions are calculated close to the instability with $U = 1.25$.

stable state followed by the extended s wave state. Close to the instability the nodeless β sheets contribute dominantly to the pairing.

Although the pairing is constrained to the close vicinity of the Fermi surfaces, one can try to find an approximation of the $g_\nu(k)$ on the different FS sheets that extends further into the Brillouin zone. Here we want to restrict ourselves to the smallest number of harmonics necessary to find a reasonable fit of the pairing function on the different FS sheets. For the s wave symmetry we can write

$$g_\nu(k) = 2A_\nu [\cos k_x + \cos k_y + 2w_{\nu,xy} \cos k_x \cos k_y + 2w_{\nu,4x4y} \cos 4k_x \cos 4k_y] \quad (35)$$

where we find for $U = 1.5$ the following parameters: $A_{\alpha_1} = 0.051$, $w_{\alpha_1,xy} = -0.35$, and $w_{\alpha_1,4x4y} = -1.35$ for the α_1 sheet, $A_{\alpha_2} = 0.02$, $w_{\alpha_2,xy} = -0.1$, and $w_{\alpha_2,4x4y} = 1$ for the α_2 sheet, and $A_\beta = 0.15$, $w_{\beta,xy} = 0.17$, and $w_{\beta,4x4y} = -0.1$ for the β sheets. In the same way, we can find an approxima-

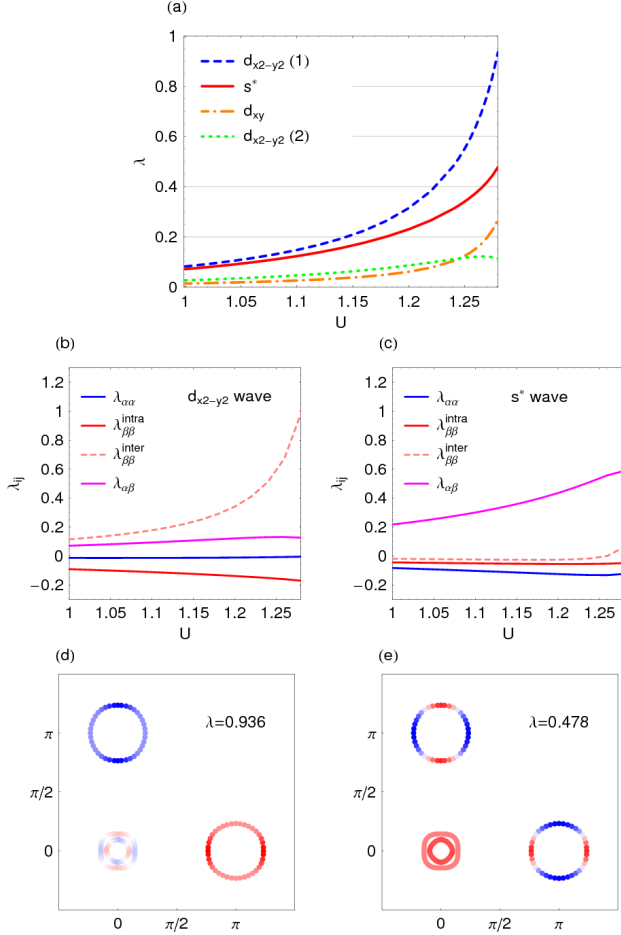


FIG. 16: (Color online) The same as in Fig. 13 for the electron-doped compound ($x = 0.125$) with $J' = J/2 = U/4$ and $V = U - 5/4J$. Here the $d_{x^2-y^2}$ wave (d) is more stable than the extended s wave (e) pairing function and the corresponding eigenvalues are clearly separated. Both are calculated close to the instability with $U = 1.28$.

tion to the d wave symmetry function as

$$g_\nu(k) = 2A_\nu [\cos k_x - \cos k_y + w_{\nu,2x}(\cos 2k_x - \cos 2k_y)] \quad (36)$$

with $A_{\alpha_1} = -1.2$ and $w_{\alpha_1,2x} = 0$ for the α_1 sheet, $A_{\alpha_2} = 0.12$ and $w_{\alpha_2,2x} = 0$, for the α_2 sheet, and $A_\beta = -0.018$ and $w_{\beta,2x} = -1.12$ for the β sheets. The results of the fitting are shown in Figs. 17 and 18.

D. Role of nesting

To study the influence of nesting on the spin susceptibility, especially on the $(\pi, 0)$ peak, we slightly modify the hopping parameters, creating a toy model with perfectly nested FS sheets. This means that we try to find an approximation where the α_2 and the β FS sheets are of approximately the same size and shape. The band structure used within this toy model is very similar to the band structure found formerly by

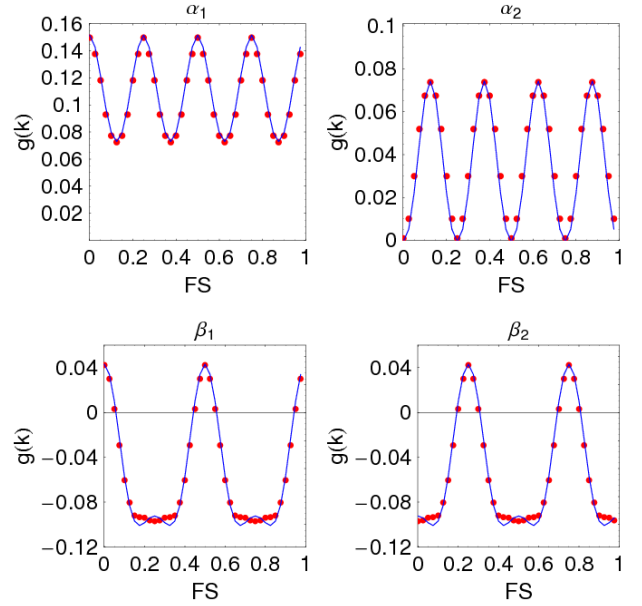


FIG. 17: (Color online) The s wave symmetry function $g(k)$ on the different FS sheets for $U = 1.5$ and $x = 0$. Here we compare a fit of $g_\nu(k)$ (blue line) to the actually calculated values of $g(k)$ (red points).

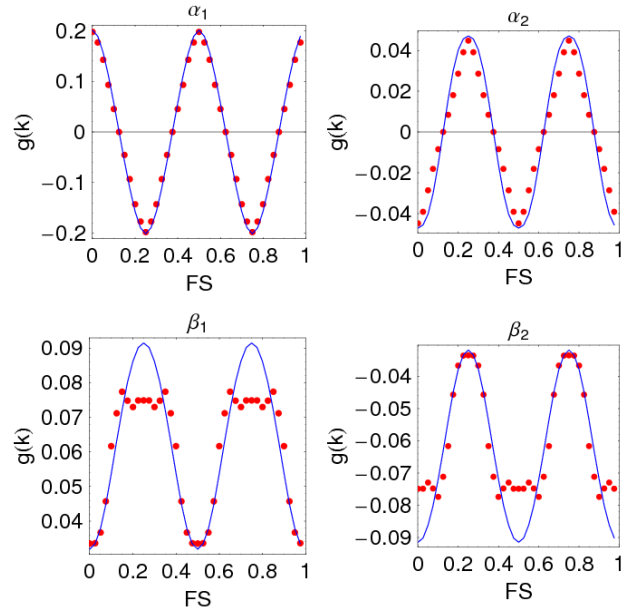


FIG. 18: (Color online) The d wave symmetry function $g(k)$ on the different FS sheets for $U = 1.5$ and $x = 0$. Here we compare a fit of $g_\nu(k)$ (blue line) to the actually calculated values of $g(k)$ (red points).

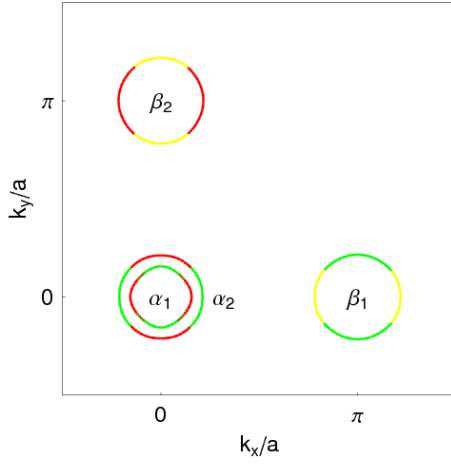


FIG. 19: (Color online) The FS sheets found within a circular approximation showing nearly perfect nesting between the α_2 and the β FS sheets with nesting vectors $(\pi, 0)$, or $(0, \pi)$, respectively. Here we use the same color convention as in Fig. 5.

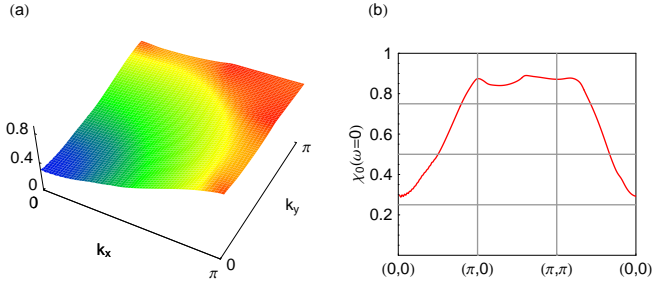


FIG. 20: (Color online) The susceptibility $\chi_0(q)$ for a toy model with spherical FS sheets.

a fit to the DFT bands, to assure that all basic properties of the model are reasonable, i.e. that the matrix elements are similar to the correct matrix elements found from the DFT fit. In Fig. 19 we show the near circular FS sheets of this model.

The bare spin susceptibility $\chi_0(q)$ for this model in the undoped case is exhibited in Fig. 20, and may be compared to the results of the original model in Fig. 7. We see that the $(\pi, 0)$ peak remains but is not particularly enhanced by the enhanced nesting, implying that the original model was already quite close to a nesting condition. On the other hand, some subtle differences which are quite interesting appear when we examine the pairing functions. If we consider an even more *Gedanken*-type model where the two α sheets have degenerate radius a , which is also the same as the two β sheets, we see that the Fermi surface in the 1st effective Brillouin zone is invariant under a translation by $(\pi, 0)$. Under this transformation, simple extended- s and $d_{x^2-y^2}$ functions $\cos k_x + \cos k_y$ and $\cos k_x - \cos k_y$ map into one another identically. We therefore expect that the pairing eigenvalues for s and $d_{x^2-y^2}$ will become degenerate. The toy model band structure considered here and shown in Fig. 19 is nearly the same as the *Gedanken* model, but has two slightly nondegenerate α sheets. We see nonetheless in Fig. 21 (b,c) and (d,e) that the two com-

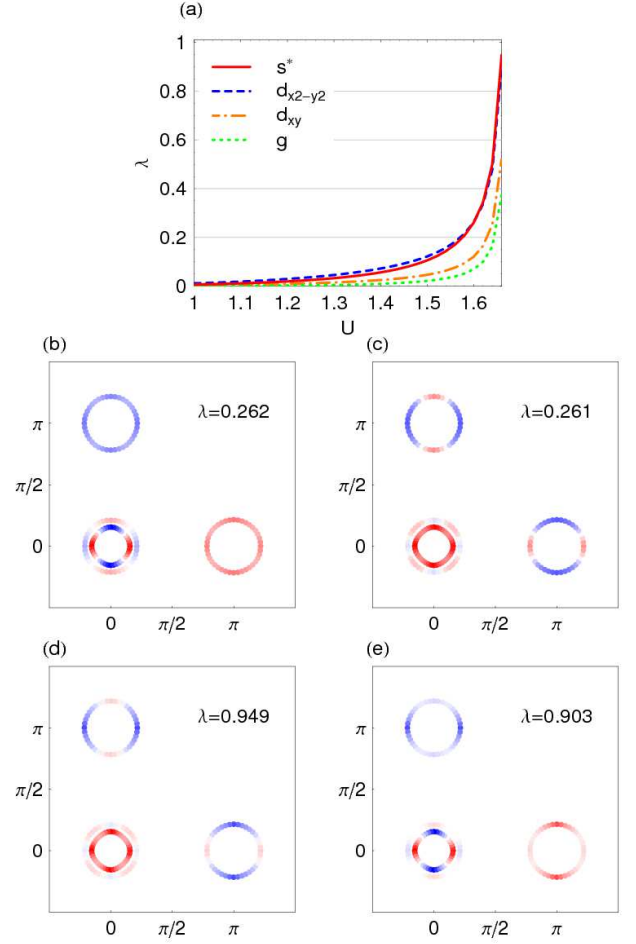


FIG. 21: (Color online) The leading eigenvalues λ for the toy model with spherical FS sheets (a). The two leading pairing functions $g(k)$ for the toy model with spherical FS sheets for $U = V = 1.6$ (b,c) and for $U = V = 1.66$ (d,e).

peting states are indeed nearly exactly degenerate. Fig. 21 (a) exhibits the dependence of the leading eigenvalues on U .

VII. THE SPATIAL AND ORBITAL STRUCTURE

The gap function $g_\nu(k)$ contains information on the spatial and orbital structure of the pairs. In the previous section, we have calculated $g_\nu(k)$ and found that its behavior on the Fermi surfaces can be fit by low order harmonics for both the s and d -wave eigenstates. Here we use these results to determine simple pictures of the internal pair structure. A gap operator can be written as

$$\Delta = \frac{1}{N} \sum_{\nu, k} g_\nu(k) \gamma_{\nu\uparrow}(k) \gamma_{\nu\downarrow}(-k) \quad (37)$$

with $\gamma_{\nu\sigma}(k)$ the destruction operator for an electron in the ν^{th} band with wave vector k and spin σ . Using the band-orbital

matrix elements to relate the band operator to the orbital operator

$$\gamma_{\nu\sigma}(k) = \sum_n a_{\nu}^n(k) d_{n\sigma}(k) \quad (38)$$

we have

$$\Delta = \frac{1}{N} \sum_{l_1, l_2} a_{nm}(l_1 - l_2) d_{n\uparrow}(l_1) d_{m\downarrow}(l_2) \quad (39)$$

with

$$a_{nm}(l) = \frac{1}{N} \sum_{k\nu} g_{\nu}(k) a_{\nu}^n(k) a_{\nu}^m(-k) e^{-ikl} \quad (40)$$

where $l = l_1 - l_2$. The amplitude $a_{nm}(l)$ describes the internal spatial and orbital structure of the pair.

Using the harmonic approximations for $g_{\nu}(k)$ for the s and $d_{x^2-y^2}$ gaps discussed in the previous section, we have calculated $a_{nm}(l)$. In principle the k sum should be cut-off when $k - k_F$ exceeds the inverse coherence length. Here we have used a Gaussian cutoff of the k sum which decays when $|\mathbf{k} - \mathbf{k}_F|$ exceeds $2\pi/\xi_0$, where ξ_0 is taken to be of order 3 times the Fe-Fe spacing a . This provides a local picture of the internal orbital structure of a pair. This basic structure continues out to a radius set by the coherence length ξ_0 .

We find that the off-diagonal amplitudes a_{nm} are negligible compared to the diagonal ones, and that the orbitals that contribute are the d_{xz} , d_{yz} , and d_{xy} orbitals which have weight near the Fermi surfaces. The amplitudes $a_{nn}(l)$ for the s and the $d_{x^2-y^2}$ gaps are shown in Figs. 22 and 23, respectively. For the s case, one sees that the internal structure of a pair consists of a superposition of $(xz \uparrow, xz \downarrow)$ singlets which are formed between a central site and sites displaced by an odd number of lattice spacings in the y -direction, $(yz \uparrow, yz \downarrow)$ singlets between the central site and odd numbered sites in the x -direction, and weaker $(xy \uparrow, xy \downarrow)$ singlets with a more intricate s -wave arrangement. The internal structure of the $d_{x^2-y^2}$ state consists of a similar superposition but with a negative phase difference between the $(xz \uparrow, xz \downarrow)$ and $(yz \uparrow, yz \downarrow)$ singlets. In addition, there is a significant $d_{x^2-y^2}$ contribution from the $(xy \uparrow, xy \downarrow)$ singlets confined primarily to the nearest neighbor sites.

VIII. SUMMARY AND CONCLUSIONS

We have studied a weak-coupling spin and charge fluctuation model of the pairing interaction using a tight-binding parametrization of the electronic band structure obtained from DFT calculations for the Fe-pnictides. We initially reviewed criticism of the 2-orbital models used in early studies of this kind, and compared results with more accurate 5-orbital models. Within the 5-orbital framework, we have calculated the multiorbital susceptibility. We calculated the static homogeneous spin susceptibility within this framework, and showed that it qualitatively agrees with experimental measurements of the T dependence, but that an interband susceptibility component was necessary to understand the magnitude of the

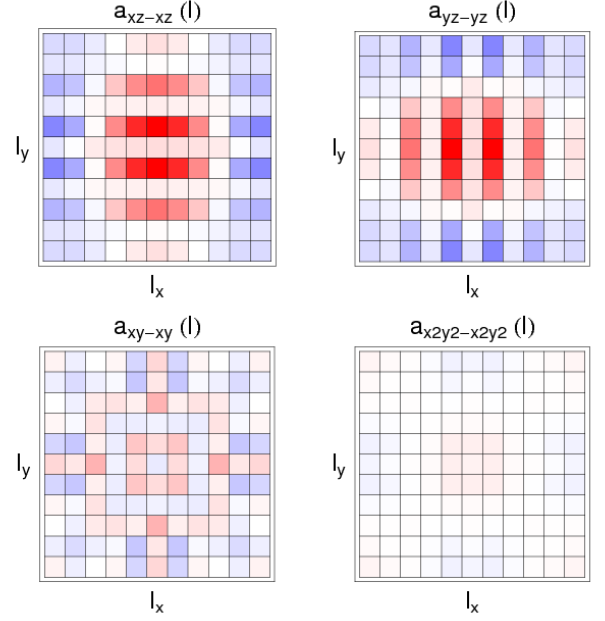


FIG. 22: (Color online) The spatial and orbital pair structure for the s gap calculated from the harmonic approximation of $g(k)$ corresponding to $U = 1.5$ with a cut-off length of $\lambda_c = 3.3d_{Fe-Fe}$.

measured low-temperature limiting susceptibility. The T -dependence of both $\chi(T)$ and $(T_1 T)^{-1}$ is qualitatively similar to experiments, and may be consistent with them for some values of the parameters. A detailed fit was not attempted here.

We then constructed the pairing vertex from the generalized RPA susceptibilities, and calculated the pairing eigenvalues for dopings corresponding to undoped and electron-doped materials, for a variety of interaction parameters corresponding to intra- and inter-orbital Coulomb matrix elements and Hund's rule couplings. We found that in the parameter region where there is a significant coupling strength, the pairing interaction for our model of the Fe-pnictides arises from the exchange of spin fluctuations. These give rise to both intra- and inter-Fermi surface scattering processes. In a number of cases the dominant pairing contribution came from particle-particle scattering processes from the hole Fermi surface around the Γ point to the electron Fermi surfaces around the $(\pi, 0)$ and $(0, \pi)$ points in the unfolded Brillouin zone. These scatterings involve momentum transfer of order $(\pi, 0)$. We find that there are two leading pairing channels, one with “sign-changing” s -wave (A_{1g}) symmetry and one with $d_{x^2-y^2}$ (B_{1g}) symmetry, and that the gap functions corresponding to both have nodes on the Fermi surface. For values of the interaction parameters corresponding to significant pairing strength, these two eigenvalues can become very close. The s -wave gap that exhibits a sign change between its average values on the electron and hole Fermi surfaces nevertheless also displays nodes on the electron sheet, whereas the d -wave state has its nodes on the hole sheet. The s -wave gap nodes are not required by symmetry, and could be absent for a different choice of parameters, but appear to be robust within the manifold of apparently re-

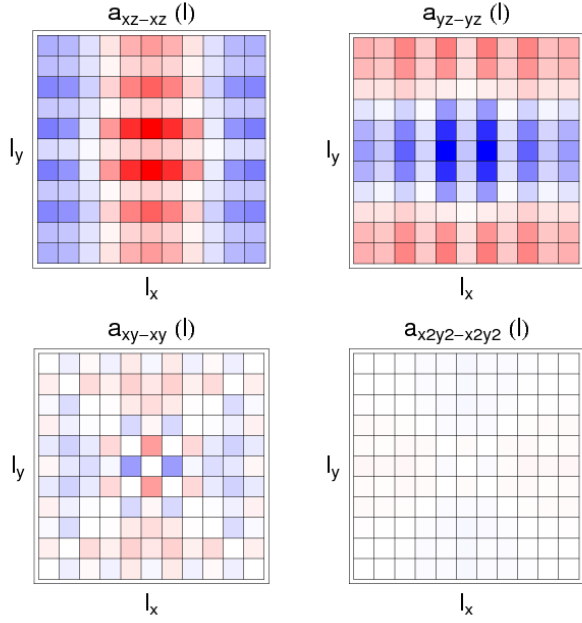


FIG. 23: (Color online) The spatial and orbital pair structure for the $d_{x^2-y^2}$ gap calculated from the harmonic approximation of $g(k)$ corresponding to $U = 1.5$ with a cut-off length of $\lambda_c = 3.3d_{Fe-Fe}$.

alistic interaction parameters we have studied.

An obvious question which arises in such studies is the sensitivity of results to the particular choice of band structure. We have relied upon the Fermi surface for the paramagnetic system determined in the Generalized Gradient Approximation (GGA) calculations of Cao *et al.*⁴, but other band calculations find subtle differences in Fermi surfaces for the La-1111 material. We have attempted to address this question by considering variations of our effective 5-band model hopping parameters chosen originally to fit the Cao *et al.* band structure. In particular, we considered variations which led to a perfect nesting of the outer α and β Fermi surface sheets, to try to maximize the $(\pi, 0)$ contribution to the pairing vertex. We found that our results for the structure of the susceptibility and pairing vertices changed in fact very little. On the other hand, the subtle changes led to a nearly exact degeneracy of the extended- s and $d_{x^2-y^2}$ eigenvalues of the linearized pairing problem. We argued that this degeneracy becomes exact for a situation where all sheets have the same radius, and propose this as a simple explanation of our finding that these two pairing channels appear to compete very strongly with one another, even in the realistic cases.

Our results appear to be qualitatively different from several works^{15,18,42,46,47} which find, on heuristic grounds or within microscopic calculations, that the A_{1g} state is closer to the form $\cos k_x \times \cos k_y$ (in the unfolded zone), in contrast to our result, which is closer to the form $\cos k_x + \cos k_y$ in the sense described above. Although both states have identical A_{1g} symmetry, the difference between them is important given the structure of the Fermi surface; for example, the $\cos k_x \times \cos k_y$ form does not have nodes on either of the β sheets shown in

Fig. 4. We believe that the strong pair scattering between the β_1 and β_2 sheets found in our calculations, and neglected in some simpler models, is crucial to stabilize the gap structure similar to $\cos k_x + \cos k_y$.

We further studied the spatial structure of the states corresponding to the leading pairing eigenvalues. In each case, the internal structure consists of a superposition of singlets made up from electrons which occupy the same d_{xz} , d_{yz} , or d_{xy} orbitals on different sites. The distribution and relative signs of these superpositions are illustrated in Figs. 22 and 23. The fact that the s -wave and d -wave solutions have very similar coupling constants opens the possibility that different members of the Fe-pnictide superconducting family may have different gap symmetries. Furthermore, it suggests that these systems may have low-lying collective particle-particle modes which would be s -wave like in a d -wave superconductor, and d -wave like in an s -wave superconductor⁴⁸.

There have been several earlier weak-coupling calculations of pairing in the Fe-pnictide superconductors. An early suggestion of an extended s -wave sign reversed gap made by Mazin *et al.*⁴² was based upon the Fermi surface structure found in a DFT calculation. There it was proposed that $(\pi, 0)$ antiferromagnetic spin fluctuations could lead to a superconducting state with an isotropic s -wave gap which had opposite signs on the electron and hole pockets.

Using a 5-orbital parameterization of the DFT bandstructure, Kuroki *et al.*¹¹ have carried out a calculation in which an RPA form for the spin and orbital contributions to the interaction was used along with bare single particle Green's functions to construct a linearized gap equation. In a parameter range similar to ours, they found that the leading pairing instability had s -wave symmetry with nodes on the electron-like Fermi surface. They also noted that the next leading channel had $d_{x^2-y^2}$ symmetry and discussed conditions under which this could become the leading pairing channel. The behavior of their s -wave gap differs from what we find by a phase factor of -1 on the electron Fermi surfaces. That is, if the gap on the inner hole Fermi surface around the Γ point is taken as positive, then Kuroki *et al.* find that the gap on the electron Fermi surface at $(\pi, 0)$ reaches its largest negative value at the point closest to the origin Γ . With the same convention, we find that the gap on the electron Fermi surface takes on its largest positive value at this point. This difference may reflect a difference in the nesting of the hole and electron Fermi surfaces due to fits to slightly different band structures or from the choice of interaction parameters⁴⁹.

Wang *et al.*¹⁹ have studied the pairing problem using a 5-orbital effective band structure together with the functional renormalization group approach. Using the same tight-binding parameterization as Kuroki *et al.*, they also find that the leading pairing channel has s -wave symmetry and that the next leading channel has $d_{x^2-y^2}$ symmetry. For their interaction parameters, they find that there are no nodes on the Fermi surface, but there is a significant variation in the magnitude of the gap. With the sign convention where the gap on the inner hole Fermi surface is positive, their gap function reaches its smallest negative value at the point on the electron Fermi surface which is closest to Γ . They note that for other parameter

choices, this s -wave gap function on the electron Fermi surface may have nodes. This would lead to a gap which becomes positive on a region of the electron Fermi surface closest to the Γ point, in agreement with what we have found.

Both of these studies also conclude that the pairing interaction arises from spin fluctuation scattering with the dominant contribution associated with $\mathbf{Q} \sim (\pi, 0)$ scattering of a pair from the inner Fermi hole surface around the Γ point to the electron Fermi surface around $(\pi, 0)$ and $(0, \pi)$. They also find that the magnitude of the gap on the central hole Fermi surface is smaller than the maximum magnitudes of the gap on the inner hole and the electron Fermi surfaces. Thus the five-orbital weak coupling calculations all find singlet pairing in the extended s -wave channel with a nearby $d_{x^2-y^2}$ wave state. The question of whether there are gap nodes for the s -wave, and indeed whether or not the s -wave state is ultimately stable with respect to the d -wave state, would both appear to depend on parameters. This sensitivity appears to us to be a natural consequence of the importance of several orbitals near the Fermi surface. In contrast to the cuprates, where calculations of this kind show a clear $d_{x^2-y^2}$ state well separated from other pairing states, it seems possible here that variations in band structure or interaction parameters found in different materials might possibly lead to different symmetry ground states.

We close by pointing out that at this writing, experiments have not conclusively answered either the question of order parameter symmetry or even whether gap nodes are present. Early indications from specific heat²¹, Andreev point contact spectroscopy²⁸, and NMR⁵⁰ on the 1111 materials suggested nodes in the superconducting order parameter. On the other hand, some penetration depth experiments³¹ and ARPES experiments^{29,32} appear to find nearly isotropic gaps in the 122 materials. Our calculations find nearly degenerate s and $d_{x^2-y^2}$ states at T_c , both of which have nodes on the Fermi surface. If the experiments indicating a lack of nodes are correct, there are two ways to imagine reconciling our conclusions with experiments on the 122 materials. The first is to consider the effects of disorder present at fairly high levels in current crystals, which should average the order parameters to a finite quasiisotropic value in the s case. The second possibility follows from the observation that if the $d_{x^2-y^2}$ state is the leading eigenvalue at T_c , the thermodynamic ground state may be unstable towards an admixture of the s state⁵¹. A similar phenomenon occurs in the phase diagram of ordinary s and

d symmetries in one-band superconductors with these pairing channels competing⁵². Separating these possibilities may be difficult, and will probably require phase sensitive probes as were discussed in the cuprate context⁵³.

Acknowledgments

This work is supported by DOE DE-FG02-05ER46236 (PJH). SG gratefully acknowledges support by the Deutsche Forschungsgemeinschaft. DJS and TAM acknowledge the Center for Nanophase Materials Sciences, which is sponsored at Oak Ridge National Laboratory by the Division of Scientific User Facilities, U.S. Department of Energy. We acknowledge useful discussions with O.K. Andersen, A. Chubukov, T. Imai, I. Mazin, X.-L. Qi and S. Raghu. We particularly thank S. Raghu for his insight regarding the interaction matrices.

APPENDIX: MODEL PARAMETERS FOR THE 5 BAND FIT

In the following, the model parameters for the 5 band tight binding fit of the DFT band structure by Cao *et al.* are listed. Including hopping up to fifth nearest neighbors on an effective Fe-Fe lattice we find intraorbital kinetic energy terms $\xi_{mm}(k)$ and interorbital kinetic terms $\xi_{mn}(k)$ that respect the basic symmetry requirements imposed by the point group of the crystal. The intra- and interband hopping parameters are given in Tab. I and Tab. II, respectively. The onsite energies ϵ_i (in eV) $\epsilon_1 = 0.13$, $\epsilon_3 = -0.22$, $\epsilon_4 = 0.3$, and $\epsilon_5 = -0.211$ where $i = 1$ corresponds to the d_{xz} , $i = 2$ to the d_{yz} , $i = 3$ to the $d_{x^2-y^2}$, $i = 4$ to the d_{xy} , and $i = 5$ to the $d_{3z^2-r^2}$ orbital, and the band structure is listed below. For the toy model with nearly spherical Fermi surface sheets we have changed t_{xy}^{11} from 0.28 to 0.3 and t_x^{13} from -0.354 to -0.409 . This is sufficient to produce nearly degenerate and spherical α_2 and β FS sheets. For the Coulomb interaction strengths we have used, the bare ratios U/t_{xy}^{11} and U/t_x^{13} are of order 5, comparable to values of U/t in the cuprates. However, we believe that for the Fe-pnictide system, the interaction is "spread out" across multiple bands leading to a substantially less strongly correlated system³⁴.

$$\begin{aligned}
\xi_{11/22} &= 2t_{x/y}^{11} \cos k_x + 2t_{y/x}^{11} \cos k_y + 4t_{xy}^{11} \cos k_x \cos k_y \pm 2t_{xx}^{11} (\cos 2k_x - \cos 2k_y) + 4t_{xxy/xyy}^{11} \cos 2k_x \cos k_y \\
&\quad + 4t_{xyy/xyx}^{11} \cos 2k_y \cos k_x + 4t_{xxyy}^{11} \cos(2k_x) \cos(2k_y) \\
\xi_{33} &= 2t_x^{33} (\cos k_x + \cos k_y) + 4t_{xy}^{33} \cos k_x \cos k_y + 2t_{xx}^{33} (\cos 2k_x + \cos 2k_y) \\
\xi_{44} &= 2t_x^{44} (\cos k_x + \cos k_y) + 4t_{xy}^{44} \cos k_x \cos k_y + 2t_{xx}^{44} (\cos 2k_x + \cos 2k_y) \\
&\quad + 4t_{xxy}^{44} (\cos 2k_x \cos k_y + \cos 2k_y \cos k_x) + 4t_{xxyy}^{44} \cos 2k_x \cos 2k_y \\
\xi_{55} &= 2t_x^{55} (\cos k_x + \cos k_y) + 2t_{xx}^{55} (\cos 2k_x + \cos 2k_y) \\
&\quad + 4t_{xxy}^{55} (\cos 2k_x \cos k_y + \cos 2k_y \cos k_x) + 4t_{xxyy}^{55} \cos 2k_x \cos 2k_y \\
\xi_{12} &= -4t_{xy}^{12} \sin k_x \sin k_y - 4t_{xxy}^{12} (\sin 2k_x \sin k_y + \sin 2k_y \sin k_x) - 4t_{xxyy}^{12} \sin 2k_x \sin 2k_y \\
\xi_{13/23} &= \pm 2it_x^{13} \sin k_{y/x} \pm 4it_{xy}^{13} \sin k_{y/x} \cos k_{x/y} \mp 4it_{xxy}^{13} (\sin 2k_{y/x} \cos k_{x/y} - \cos 2k_{x/y} \sin k_{y/x}) \\
\xi_{14/24} &= 2it_x^{14} \sin k_{x/y} + 4it_{xy}^{14} \cos k_{y/x} \sin k_{x/y} + 4it_{xxy}^{14} \sin 2k_{x/y} \cos k_{y/x} \\
\xi_{15/25} &= 2it_x^{15} \sin k_{y/x} - 4it_{xy}^{15} \sin k_{y/x} \cos k_{x/y} - 4it_{xxyy}^{15} \sin 2k_{y/x} \cos 2k_{x/y} \\
\xi_{34} &= 4t_{xxy}^{34} (\sin 2k_y \sin k_x - \sin 2k_x \sin k_y) \\
\xi_{35} &= 2t_x^{35} (\cos k_x - \cos k_y) + 4t_{xxy}^{35} (\cos 2k_x \cos k_y - \cos 2k_y \cos k_x) \\
\xi_{45} &= 4t_{xy}^{45} \sin k_x \sin k_y + 4t_{xxyy}^{45} \sin 2k_x \sin 2k_y
\end{aligned}$$

t_i^{mn}	$i = x$	$i = y$	$i = xy$	$i = xx$	$i = xxy$	$i = xyy$	$i = xxyy$
$m = 1$	-0.14	-0.4	0.28	0.02	-0.035	0.005	0.035
$m = 3$	0.35		-0.105	-0.02			
$m = 4$	0.23		0.15	-0.03	-0.03		-0.03
$m = 5$	-0.1			-0.04	0.02		-0.01

TABLE I: The intraorbital hopping parameters used for the DFT fit of the 5 orbital model.

t_i^{mn}	$i = x$	$i = xy$	$i = xxy$	$i = xxyy$
$mn = 12$		0.05	-0.015	0.035
$mn = 13$	-0.354	0.099	0.021	
$mn = 14$	0.339	0.014	0.028	
$mn = 15$	-0.198	-0.085		-0.014
$mn = 34$			-0.01	
$mn = 35$	-0.3		-0.02	
$mn = 45$		-0.15		0.01

TABLE II: The interorbital hopping parameters used for the DFT fit of the 5 orbital model.

-
- ¹ W. Malaeb, T. Yoshida, T. Kataoka, A. Fujimori, M. Kubota, K. Ono, H. Usui, K. Kuroki, R. Arita, H. Aoki, Y. Kamihara, M. Hirano and H. Hosono *J. Phys. Soc. Jpn.* **77** (2008) 093714.
- ² S. Lebègue, *Phys. Rev. B* **75**, 035110 (2007).
- ³ D.J. Singh and M.-H. Du, *Phys. Rev. Lett.* **100**, 237003 (2008).
- ⁴ C. Cao, P.J. Hirschfeld, H.-P. Cheng, *Phys. Rev. B* **77**, 220506(R) (2008).
- ⁵ O.K. Andersen, private communication.
- ⁶ J. Dong, H.J. Zhang, G. Xu, Z. Li, G. Li, W.Z. Hu, D. Wu, G.F. Chen, X. Dai, J.L. Luo, Z. Fang and N.L. Wang, *Europhys. Lett.* **83**, 27006 (2008).
- ⁷ C. de la Cruz, Q. Huang, J.W. Lynn, J. Li, W. Ratcliff, J.L. Zarestky, H.A. Mook, G.F. Chen, J.L. Luo, N.L. Wang, and P. Dai, *Nature* **453**, 899 (2008).
- ⁸ J. Zhao, Q. Huang, C. de la Cruz, S. Li, J.W. Lynn, Y. Chen, M.A. Green, G.F. Chen, G. Li, Z. Li, J.L. Luo, N.L. Wang, and P. Dai, *Nature Materials* **7**, 953 (2008).
- ⁹ H. Luetkens, H.-H. Klauss, M. Kraken, F.J. Litterst, T. Dellmann, R. Klingeler, C. Hess, R. Khasanov, A. Amato, C. Baines, J. Hamann-Borrero, N. Leps, A. Kondrat, G. Behr, J. Werner,

- B. Buechner, arXiv:0806.3533.
- ¹⁰ A.J. Drew, Ch. Niedermayer, P.J. Baker, F.L. Pratt, S.J. Blundell, T. Lancaster, R.H. Liu, G. Wu, X.H. Chen, I. Watanabe, V.K. Malik, A. Dubroka, M. Rössle, K.W. Kim, C. Baines and C. Bernhard, arXiv:0807.4876.
- ¹¹ K. Kuroki, S. Onari, R. Arita, H. Usui, Y. Tanaka, H. Kontani and H. Aoki, Phys. Rev. Lett. **101**, 087004 (2008).
- ¹² X.-L. Qi, S. Raghu, C.-X. Liu, D.J. Scalapino and S.-C. Zhang, arXiv:0804.4332.
- ¹³ V. Barzykin and L.P. Gorkov, arXiv:0806.1933.
- ¹⁴ Y. Bang and H.-Y. Choi, Phys. Rev. B **78**, 134523 (2008).
- ¹⁵ Y. Yanagi, Y. Yamakawa, and Y. Ono, arXiv:0808.1192; arXiv:0809.3189.
- ¹⁶ Z.-J. Yao, J.-X. Li and Z.D. Wang, arXiv:0804.4166.
- ¹⁷ R. Sknepnek, G. Samolyuk, Y. Lee, B.N. Harmon and J. Schmalian, arXiv:0807.4566.
- ¹⁸ H. Ikeda, arXiv:0810.1828.
- ¹⁹ F. Wang, H. Zhai, Y. Ran, A. Vishwanath and D.-H. Lee, arXiv:0807.0498.
- ²⁰ A.V. Chubukov, D. Efremov and I. Eremin, Phys. Rev. B **78**, 134512 (2008).
- ²¹ G. Mu, X.-Y. Zhu, L. Fang, L. Shan, C. Ren and H.-H. Wen, Chin. Phys. Lett. **25**, 2221 (2008); arXiv:0803.0928.
- ²² K. Matano, Z.A. Ren, X.L. Dong, L.L. Sun, Z.X. Zhao, G. Zheng, Europhys. Lett. **83**, 57001 (2008).
- ²³ H. Mukuda, N. Terasaki, H. Kinouchi, M. Yashima, Y. Kitaoka, S. Suzuki, S. Miyasaka, S. Tajima, K. Miyazawa, P.M. Shirage, H. Kito, H. Eisaki, A. Iyo, arXiv:0806.3238.
- ²⁴ Y. Nakai, K. Ishida, Y. Kamihara, M. Hirano, H. Hosono, arXiv:0804.4765.
- ²⁵ T.Y. Chen, Z. Tesanovic, R.H. Liu, X.H. Chen, C.L. Chien, *Nature* **453**, 1224 (2008); K.A. Yates, L.F. Cohen, Z.-A. Ren, J. Yang, W. Lu, X.-L. Dong, Z.-X. Zhao, Supercond. Sci. Technol. **21**, 092003 (2008).
- ²⁶ T. Kondo, A.F. Santander-Syro, O. Copie, C. Liu, M.E. Tillman, E.D. Mun, J. Schmalian, S.L. Bud'ko, M.A. Tanatar, P.C. Canfield, A. Kaminski, Phys. Rev. Lett. **101**, 147003 (2008).
- ²⁷ G. Li, W.Z. Hu, J. Dong, Z. Li, P. Zheng, G.F. Chen, J.L. Luo, N.L. Wang, Phys. Rev. Lett. **101**, 107004 (2008).
- ²⁸ L. Shan, Y. Wang, X. Zhu, G. Mu, L. Fang, C. Ren and H.-H. Wen, Europhys. Lett. **83**, 57004 (2008).
- ²⁹ D.V. Evtushinsky, D.S. Inosov, V.B. Zabolotnyy, A. Koitzsch, M. Knupfer, B. Buchner, G.L. Sun, V. Hinkov, A.V. Boris, C.T. Lin, B. Keimer, A. Varykhalov, A.A. Kordyuk, S.V. Borisenko, arXiv:0809.4455.
- ³⁰ C. Martin, R.T. Gordon, M.A. Tanatar, M.D. Vannette, M.E. Tillman, E.D. Mun, P.C. Canfield, V.G. Kogan, G.D. Samolyuk, J. Schmalian, R. Prozorov, arXiv:0807.0876.
- ³¹ K. Hashimoto, T. Shibauchi, S. Kasahara, K. Ikada, T. Kato, R. Okazaki, C.J. van der Beek, M. Konczykowski, H. Takeya, K. Hirata, T. Terashima, Y. Matsuda, arXiv:0810.3506.
- ³² H. Ding, P. Richard, K. Nakayama, T. Sugawara, T. Arakane, Y. Sekiba, A. Takayama, S. Souma, T. Sato, T. Takahashi, Z. Wang, X. Dai, Z. Fang, G.F. Chen, J.L. Luo, N.L. Wang, Europhys. Lett. **83**, 47001 (2008).
- ³³ P.A. Lee and X.-G. Wen, arXiv:0804.1739.
- ³⁴ V.I. Anisimov, Dm.M. Korotin, M.A. Korotin, A.V. Kozhevnikov, J. Kunes, A.O. Shorikov, S.L. Skornyakov, and S.V. Streltsov, arXiv:0810.2629.
- ³⁵ A.M. Olés, Phys. Rev. B **28**, 327 (1983).
- ³⁶ T. Takimoto, T. Hotta, and K. Ueda, Phys. Rev. B **69**, 104504 (2004).
- ³⁷ K. Kubo, Phys. Rev. B **75**, 224509 (2007).
- ³⁸ R. Klingeler, N. Leps, I. Hellmann, A. Popa, C. Hess, A. Kondrat, J. Hamann-Borrero, G. Behr, V. Kataev, and B. Buechner, arXiv:0808.0708.
- ³⁹ H.-J. Grafe, D. Paar, G. Lang, N.J. Curro, G. Behr, J. Werner, J. Hamann-Borrero, C. Hess, N. Leps, R. Klingeler, and B. Buchner, Phys. Rev. Lett. **101**, 047003 (2008).
- ⁴⁰ K. Ahilan, F.L. Ning, T. Imai, A.S. Sefat, R. Jin, M.A. McGuire, B.C. Sales, D. Mandrus, Phys. Rev. B **78**, 100501(R) (2008).
- ⁴¹ G.-M. Zhang, Y.-H. Su, Z.-Y. Lu, Z.-Y. Weng, D.-H. Lee, T. Xi-ang, arXiv:0809.3874.
- ⁴² I.I. Mazin, D.J. Singh, M.D. Johannes and M.H. Du, Phys. Rev. Lett. **101**, 057003 (2008).
- ⁴³ N.E. Bickers, D.J. Scalapino and S.R. White, Phys. Rev. Lett. **62**, 961 (1989).
- ⁴⁴ D.J. Scalapino, E. Loh, Jr., and J.E. Hirsch, Phys. Rev. B **34**, 8190 (1986).
- ⁴⁵ We find that in order to generate pairing eigenvalues of order 1, we need to work within the RPA at interaction strengths quite close to the Stoner instability. However, from earlier experience comparing RPA with quantum Monte Carlo results on the single-band Hubbard model (T.A. Maier *et al.*, Phys. Rev. B **76**, 144516 (2007)), we expect that the bare interaction parameters appearing in the RPA expressions are renormalized, such that one is actually not so close to the true instability.
- ⁴⁶ S.-L. Yu, J. Kang, and J.-X. Li, arXiv:0901.0821.
- ⁴⁷ M.M. Parish, J. Hu, and B.A. Bernevig, Phys. Rev. B **78**, 144514 (2008).
- ⁴⁸ A. Bardasis, and J.R. Schrieffer, Phys. Rev. **121**, 1050 (1961).
- ⁴⁹ Note: Even when taking the band parameters given in Kuroki *et al.* and identical interaction parameters, we find a different Fermi surface and pairing eigenvalues. Also the extended *s* wave pairing function we find for these parameters differs from the one found by Kuroki *et al.* In contrast to this work Kuroki *et al.* use a dynamical susceptibility, but it seems unlikely that this could account for these differences.
- ⁵⁰ F. Ning, K. Ahilan, T. Imai, A.S. Sefat, R. Jin, M.A. McGuire, B.C. Sales, and D. Mandrus, J. Phys. Soc. Jpn. **77** 103705 (2008).
- ⁵¹ W.-C. Lee, S.-C. Zhang and C. Wu, arXiv:0810.5114.
- ⁵² K.A. Muesalian, J. Betouras, A.V. Chubukov, and R. Joynt, Phys. Rev. B **53**, 3598 (1996).
- ⁵³ C.C. Tsuei and J.R. Kirtley, Rev. Mod. Phys. **72**, 969 (2000).